Chapter 4

Underglaze pigments on shards and plates

This chapter deals with the study of underglaze pigments on blue and white shards originating from a museum, as well as those excavated in and around the city of Tshwane, South Africa. The museum and excavated shards (of known and unknown origin) are from the National Cultural History Museum (NCHM) of South Africa. Two intact Ming plates provided by the J.A. van Tilburg Museum at the University of Pretoria were also studied for comparison. This chapter concludes by highlighting the major results and the implications of these results for art and archaeological research. Some of the work in this chapter has recently been published in the *Journal of Raman Spectroscopy*.[1]

4.1 Glaze depth profiling

The objective was to obtain clear Raman spectra from the ceramic/glaze interfacial region by focusing the laser beam through the glaze for excitation, while collecting the Raman scattered radiation from that interface in the 180^{o} scattering configuration. Since the bulk of the fluorescence emanates from the intervening glaze, the focus point was systematically varied by 4 μm in the vertical axis (Z-axis) starting at the glaze surface, while keeping both the X and Y-axis positions constant and acquiring a spectrum at each position. In this way, a vertical profile of the glaze was generated.[1] Figure 4.1 shows a schematic view of the focus positions for both the glaze surfaces and the ceramic/glaze interface, with the laser powers required for the various thicknesses of the glazes that were studied.

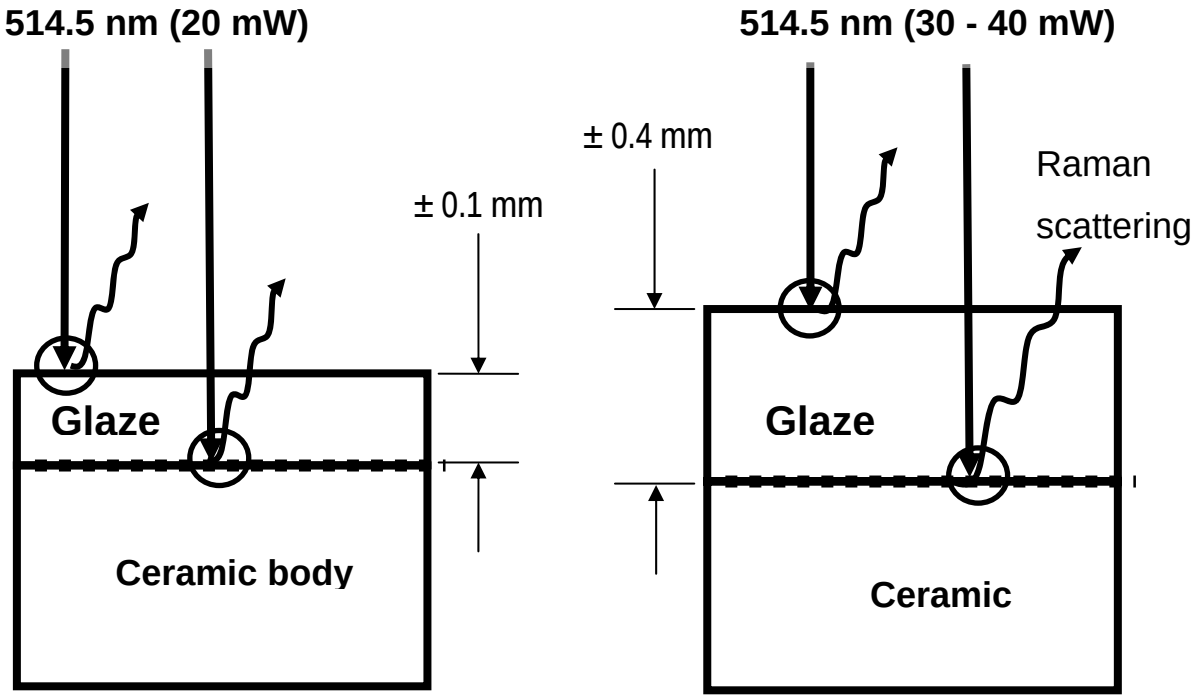

Figure 4.1.1. Schematic view of the focus positions for both the glaze surfaces and the ceramic/glaze interface

Figure 4.1.1 shows that for glaze thicknesses of up to 100 µm, 20 mW was sufficient to obtain ceramic/glaze interfacial spectra, while for thicker glazes of up to 400 µm, higher laser powers (40 mW) were required.

Obtaining spectra through the glaze in this way permits the study of underglaze pigments on intact glazed ceramic artifacts where the pigment is not exposed to the surface for direct study. Figure 4.1.2 shows a typical positioning of an intact museum artifact (in this case a plate) in order to generate a glaze depth profile on an intact museum sample. Figure 4.1.3 shows the first set of samples that were chosen for Raman analysis of underglaze pigments by focusing the excitation radiation through the glaze.

Figure 4.1.2. Typical positioning of a precious porcelain museum piece for glaze depth profile studies using micro-Raman spectroscopy (unknown plate from the J.A. van Tilburg Museum, University of Pretoria)

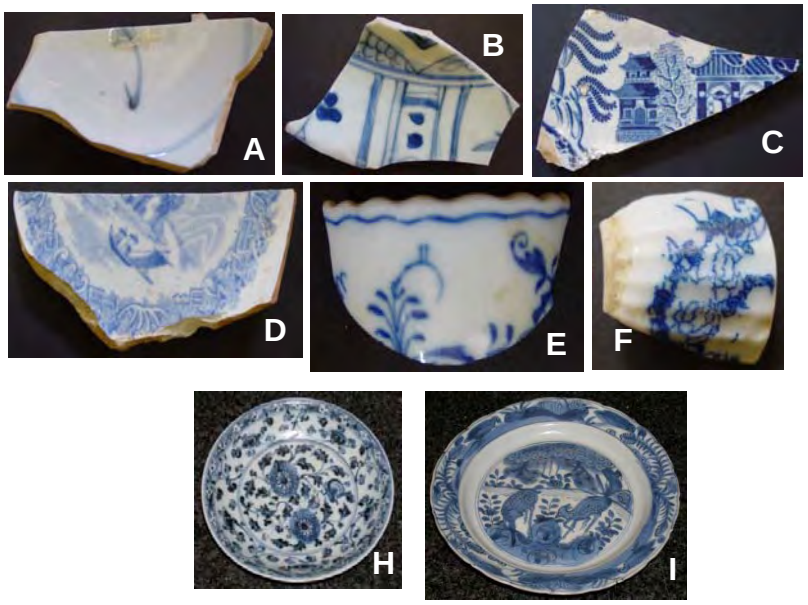

Figure 4.1.3. The set of samples chosen for this study is shown. Samples A and B are of Ming dynasty origin; samples C, D and F are archaeological samples; sample E is of Meissen origin; and samples H and I are intact Ming plates

4.2. Ceramic/glaze interfacial structure

The structure of the ceramic/glaze interfaces is sometimes difficult to characterise by directing the beam at broken surfaces (in the case of broken artifacts) as often the layers are extremely thin and it is therefore difficult to distinguish the order in which the materials were applied on the surface at the time of manufacture, if one can detect them at all. In the case of intact ceramic artifacts where the pigment is not exposed to the surface, this task becomes impossible without going through the glaze using regular techniques. However, using the glaze depth profiling method, one can easily characterise the ceramic/glaze interfacial region. Figure 4.2.1. and Figure 4.2.2.) shows the raw (no filtering or baseline corrections) Raman spectra, illustrating the incremental interval profile needed to characterise the interface.

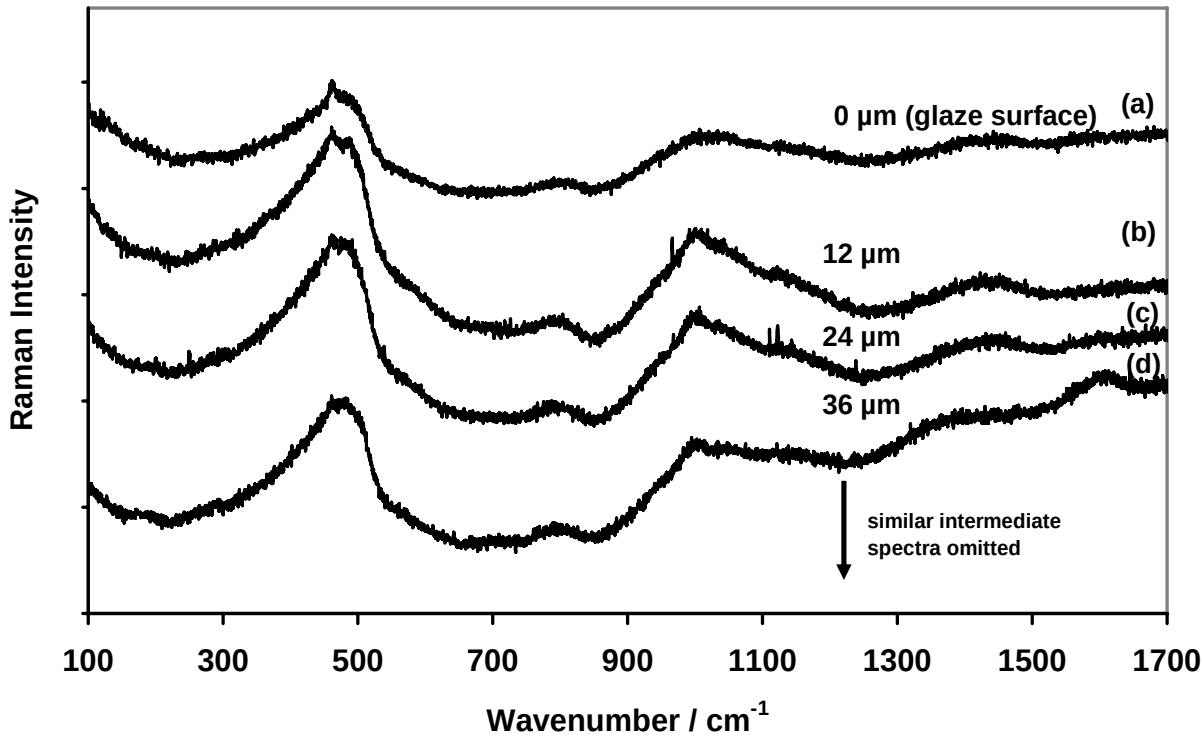

Figure 4.2.1 Typical raw Raman spectra. The surface spectrum in (a) at 0 µm shows only the glaze, while going deeper into the glaze shows a clear pigment spectrum from (f) to (h) as illustrated in Figure 4.2.2. on the following page.

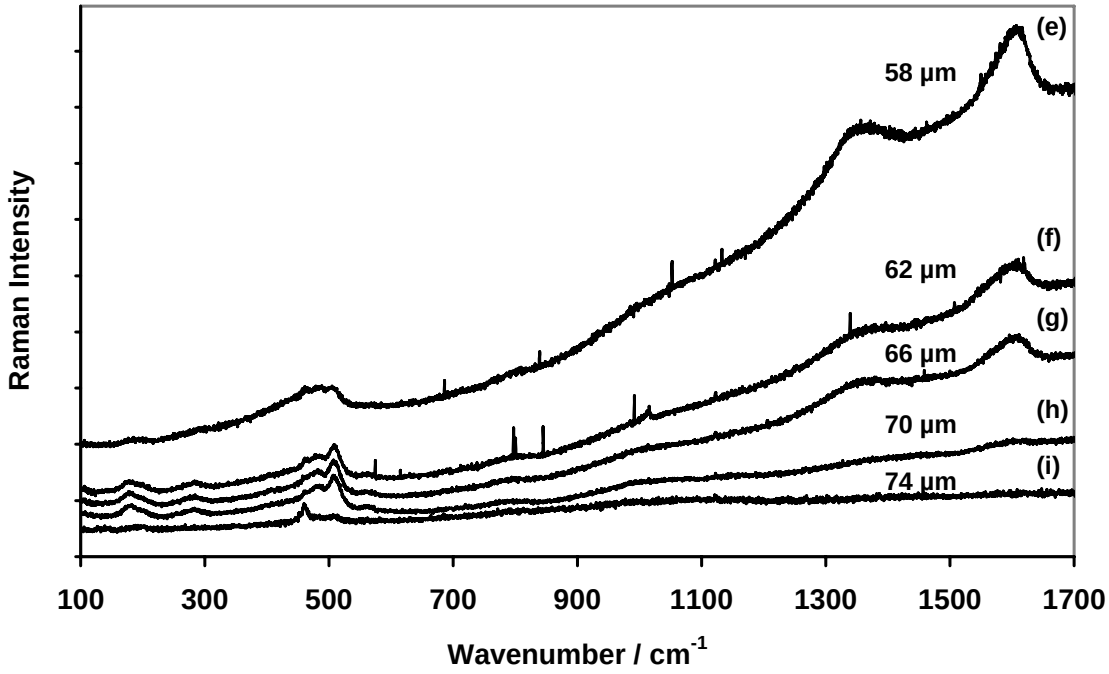

Figure 4.2.2. The spectra from (e) to (i) is a continuation from Figure 4.2.1. This part shows spectra deeper into the glaze from 58 µm to 74 µm at same vertical position. Note the amorphous carbon bands around 1300 and 1600 cm^{-1} from (e) to (g)

From spectra in Figure 4.2.1 and Figure 4.2.2, one can easily construct the structure of the interface. Firstly, the top layer shows the Raman spectra emanating from the glaze [(a) to (d)]. Note that many more spectra collected from the glaze as the interface is approached are not included. Secondly, just as the laser beam strikes the pigment layer [Figure 4.2.2(e) to (h)], strong amorphous carbon bands are observed around 1300 cm^{-1} and 1600 cm^{-1}, indicating a mixture of pigments (cobalt blue and amorphous carbon). As the beam passes the pigment layer and strikes the quartz-dominated ceramic surface, a strong band at 461 cm^{-1} appears. One of the key features of these spectra is the fluorescence intensity that is clearly higher in the glaze layer as well as in this particular pigment layer, but dies off as the laser beam reaches the quartz layer. Figure 4.2.3 illustrates the interfacial structure for this sample (unknown sample C).

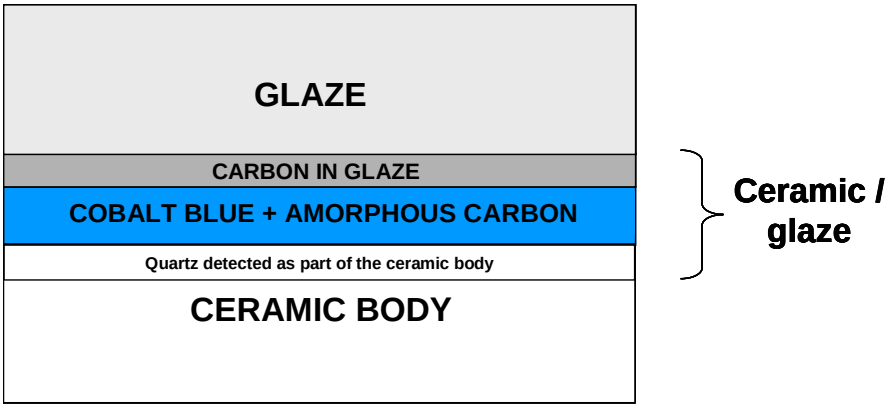

Figure 4.2.3. Schematic view of the ceramic/glaze interfacial region as determined through generating a typical glaze profile with micro-Raman spectroscopy on dark blue sections of sample C (see Figure 4.1.3)

Figure 4.2.4 shows the Raman glaze depth profile from which the schematic view of the ceramic/glaze interfacial region in Figure 4.2.5 was generated.

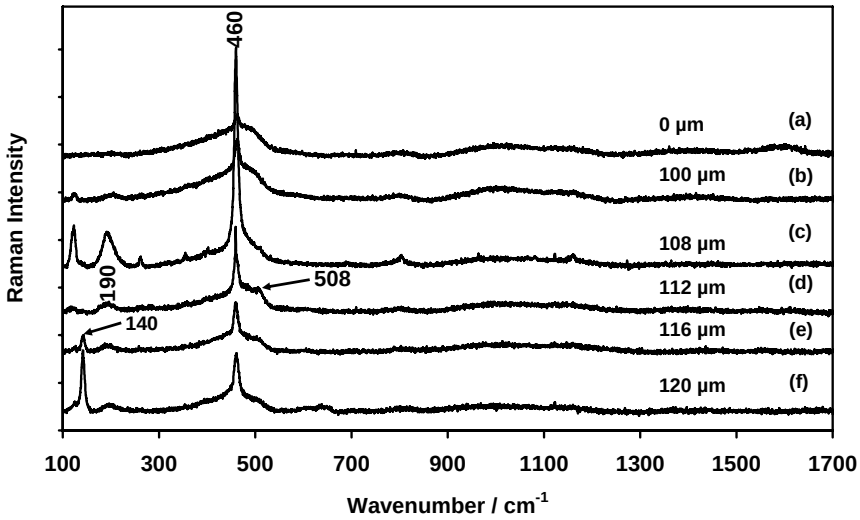

Figure 4.2.4. Raman spectra in which the glaze surface spectrum in (a) at 0 µm shows only the glaze. The spectra shown from 100 to 120 µm for this sample D (unknown shard) typically show the spectral evolution of the interfacial region

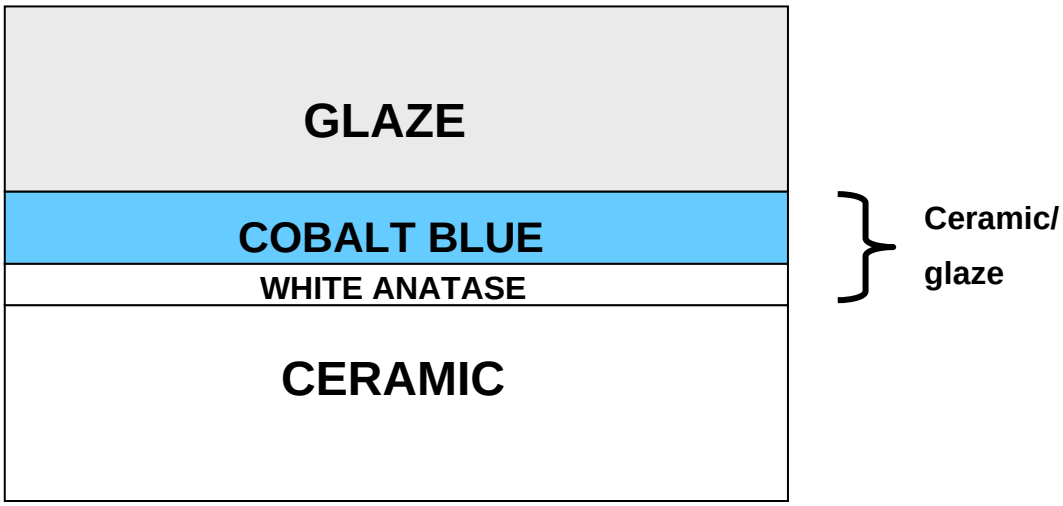

Figure 4.2.5. Schematic view of the ceramic/glaze interfacial region as determined from the Raman glaze profile in Figure 4.2.4

Figure 4.2.5 shows the order in which the pigments were applied on the artifact [sample D (of unknown archaeological origin)] at the time of manufacture. The order shown here suggests that the white anatase was applied first before the blue pigment. This suggests a deliberate intention to whiten the artifact before decorations with cobalt blue pigment were undertaken in order to create better pigment and surface background contrast, thus giving some insight into the methods used by the manufacturers of the artifact.

The identification of the white anatase itself on this artifact tells its own story. First, since white anatase is known to have been manufactured[2] for the first time during the 1920s, this artifact could not be of ancient Ming or non-Ming origin. The implication for the site where the artifact was excavated is that it is unlikely to be

older than the oldest piece found in it. This line of reasoning should then add value to work done by archaeologists in dating archaeological sites.

4.3. Identification of pigments, characterisation and implications

A description of the identified pigments will be given in this section. This will be accompanied by a detailed analysis of each pigment as it is found on the artifacts. The implications of its presence in relation to art and archaeology will also be discussed. It should be noted, for example, that a new synthetic pigment that is found on an artifact presented as an invaluable ancient artifact immediately raises questions,[3] especially when these artifacts are traded at high prices. Also, the correct dating of ancient artifacts invariably benefits discussions on history and archaeology.[4]

4.3.1. Cobalt aluminium oxide ($CoAl_2O_4$)

Cobalt aluminium oxide ($CoAl_2O_4$) also known as cobalt blue, is the origin of the blue colour on all the shards studied. Cobalt blue belongs to a class of compounds generally characterised by a cation in an octahedral position (A) and another cation in a tetrahedral position [B], such that they can be represented as $(A_{1-x}B_x)[A_xB_{2-x}]O_4$ and $0 \leq x \leq 1$. For the normal spinels, $x = 0$, such that we obtain $(A)[B_2]O_4$. For all other $0 < x \leq 1$, we get many different types of inverse spinel.[1]

Cobalt blue finds applications as a colorant in a variety of industries such as plastics, paint, fibres, paper, rubber, glass and cement.[5] Other applications include glazes, ceramic bodies, porcelain enamels and as contrast-enhancing luminescent pigment in TV tubes.[1,5,6] It is a very stable pigment with a long history of use in ceramic artifacts, both ancient and modern. Spinels such as cobalt blue belong to a ceramic oxide family with wide applications in geophysics,[4] magnetism,[5] irradiated

environments,[6,7] as well as colour enhancers.[8,9] Yet, until recently,[10] the cobalt blue Raman spectrum within ceramic artifacts had not been determined.

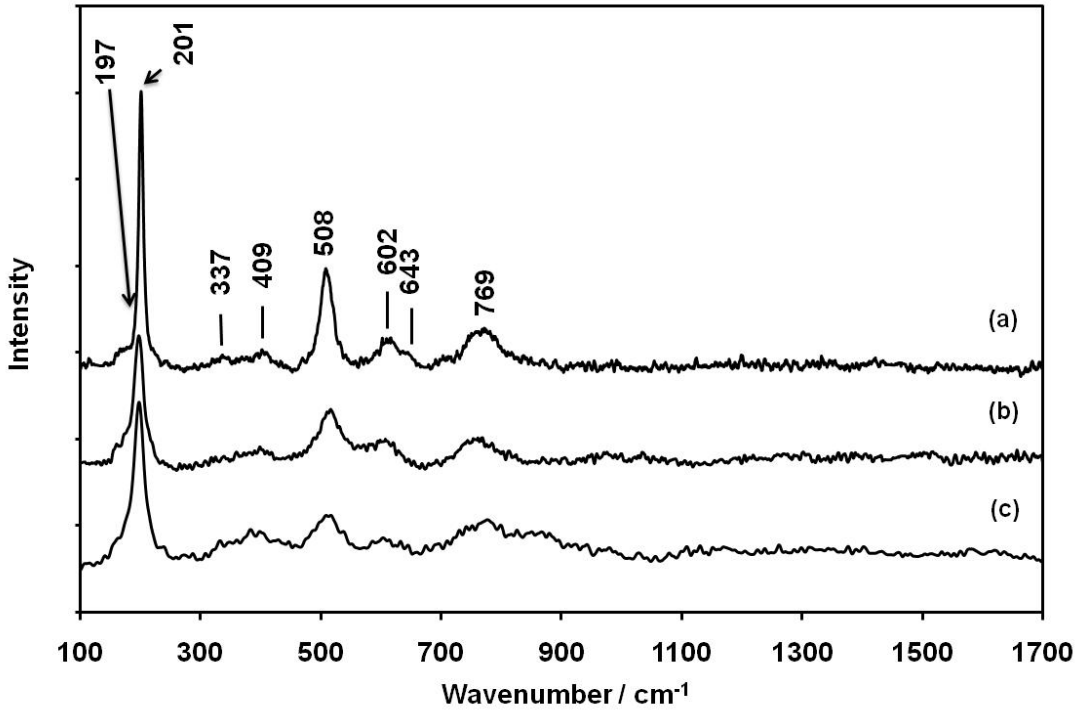

Figure 4.3.1.1. The Raman spectra of cobalt blue cooled rapidly (a), cooled slowly (b) and a commercial sample (c); the commercial sample was supplied by *Farbmühle Kraemer* in Germany and was used as received

Figure 4.3.1.1. shows the Raman spectra of cobalt blue cooled rapidly (a), cobalt blue cooled slowly (b), and a commercial sample of cobalt blue used as received (*Farbmühle Kraemer*, Germany) is shown in (c).

As a normal spinel structured pigment, cobalt blue belongs to space group F*d3m* O^7_h with 56 atoms per unit cell (Z = 8).[11,12] Group theory, which is a branch of abstract mathematics, is applied widely in the physical sciences. This theory is used here to develop vibrational selection rules for the blue pigment ($CoAl_2O_4$), thereby determining the number of expected vibrations within the pigment crystal. The

application of group theory will be focused on obtaining vibrational information as it relates to Raman and infrared spectroscopy. It may be noted here that group theory can also be applied in chemistry to obtain other physical properties such as parity, chirality of molecules and the construction of molecular orbitals.[13] In the study of Raman and infrared spectroscopy, point groups are used to determine the normal modes of vibration and the relevant selection rules. A well-defined and well-known correlation method, clearly documented by Fateley and co-workers[13] is used to derive the total number of vibrational modes for cobalt aluminium oxide ($CoAl_2O_4$).

The procedure of the correlation method begins by determining the degrees of vibrational freedom (f^{γ}) in each site species for γ of an equivalent set of atoms using:

$$f^{\gamma} = t^{\gamma}. n \qquad 4.1$$

where t^{γ} = number of translations in site species γ

n = number of atoms in an equivalent set

The degrees of vibrational freedom (f^{γ}) from each site species γ that are calculated are then used to determine the degrees of freedom (a_{γ}) that are contributed by each site species γ to the factor group ζ, as follows:

$$f^{\gamma} = a_{\gamma} \sum_{\zeta} C_{\zeta} \qquad 4.2$$

where C_{ζ} is the degeneracy of the species ζ of the factor group.

Table 4.3.1.1 lists the values of C_{ζ}.

Table 4.3.1.1. The values of the species that are chosen are shown below and depend on the type of crystal or molecule being considered.

Species	Value of C_ζ
A	1
B	1
E	2
T	3
G	4
H	5

It is from this list that specific values for a particular symmetry species are chosen, depending on the type of crystal under consideration. The use of these symbols (known as Mulliken symbols) and the symmetry properties that they represent are well known.[14]

The degrees of freedom contributed from each site species (a_γ) to the degrees of freedom (a_ζ) of the factor group may now be written directly as:

$$a_\zeta = \sum_\gamma a_\gamma \qquad 4.3$$

The construction of the irreducible representation for each equivalent set of atoms ($\Gamma_{\text{equivalent set}}$), in this case cobalt (Co), aluminium (Al) and oxygen (O), follows directly by summing the product of the factor group and its degrees of freedom obtained from equation 4.3:

$$\Gamma_{\text{equivalent set}} = \sum_\zeta a_\zeta \, \zeta \qquad 4.4$$

The total irreducible representation ($\Gamma^{crystal}$) is simply the sum of irreducible representations for each equivalent set:

$$\Gamma^{crystal} = \Gamma_{equivalent\ set\ (Co)} + \Gamma_{equivalent\ set\ (Al)} + \Gamma_{equivalent\ set\ (O)} \qquad 4.5$$

By subtracting the acoustic modes, $\Gamma^{acoustic}$, we obtain the total irreducible representation of the pigment crystal:

$$\Gamma^{CoAl_2O_4}_{Vibration} = \Gamma^{crystal} - \Gamma^{acoustic} \qquad 4.6$$

The crystal structure of $CoAl_2O_4$ belongs to space group F*d*3*m* (O^7_h) with 56 atoms per unit cell (Z = 8)[11,12] where Z is the number of molecular units per unit cell. The number of molecular units per Bravais cell (Z^B) is Z^B = Z / L.P, where L.P. is the number of lattice points in F*d*3*m* (O^7_h) that can be determined. This is done in order to reduce the number of Bravais cells in the crystallographic cell, thereby ensuring that the obtained irreducible representations do not contain multiples of the set of vibrations needed to describe the crystal. From this information, it follows that the number of equivalent atoms may be listed as Co = 2, Al = 4 and O = 8.

Using information from site symmetry tables for the Bravais space cell, character tables and correlation tables,[14] it was possible to derive an equation for the expected number of normal modes in the crystalline cobalt aluminium oxide. The Bravais space cell site symmetries are all the possible kinds of site for the particular crystal symmetry (for example, O^7_h). Table 4.3.1.2 gives a list of the O^7_h site symmetry species that have been used for the $CoAl_2O_4$ crystal.

Table 4.3.1.2. The distinct kinds of T_d, D_{3d} and C_{3v} sites and the number of equivalent atoms that can occupy each distinct site within the same distinct kind of site

Bravais cell site symmetry	Number of equivalent atoms on this site of the Bravais cell	Number of kinds of site of this symmetry
$2T_d(2)$	2	2
$2D_{3d}(4)$	4	2
$C_{3v}(8)$	8	1

From Table 4.3.1.2, only two distinct kinds of T_d site can accommodate two equivalent atoms. We therefore conclude that the site symmetry for Co (cobalt) is T_d (n = 2) where n is the number of atoms in an equivalent set. Similarly, site symmetry for Al (aluminium) is D_{3d} (n = 4) and that for O (oxygen) is C_{3v} (n = 8).

Table 4.3.1.3. Aluminium atom site D_{3d}, with the degree of vibrational freedom for each species (n = 4 atoms / equivalent set)

D_{3d} species	Translations	t^γ	Degree of vibrational freedom: $f^\gamma = n.t^\gamma$
A_{1g}		0	0
A_{2g}		0	0
E_g		0	0
A_{1u}		0	0
A_{2u}	T_z	1	4
E_u	T_x, T_y	2	8

Table 4.3.1.4. Cobalt atom site T_d, with the degree of vibrational freedom for each species (n = 2 atoms / equivalent set)

T_d species	Translations	t^γ	Degree of vibrational freedom: $f^\gamma = n.t^\gamma$
A_1		0	0
A_2		0	0
E		0	0
T_1		0	0
T_2	T_x, T_y, T_z	3	6

Table 4.3.1.5. Oxygen atom site C_{3v}, with the degree of vibrational freedom for each species (n = 8 atoms / equivalent set)

C_{3v} species	Translations	t^γ	Degree of vibrational freedom: $f^\gamma = n.t^\gamma$
A_1	T_z	1	8
A_2		0	0
E	T_x, T_y	2	16

Once the degrees of vibrational freedom have been determined in this manner, the correlation table can be completed from T_d, D_{3d} and C_{3v} to O^7_h Tables 4.3.1.6, 4.3.1.7 and 4.3.1.8 complete these correlations using abbreviated tables dealing only with species that are involved in the $CoAl_2O_4$ crystal.

Table 4.3.1.6. Correlation between the D_{3d} site group and the O^7_h factor group for the aluminium atoms (n = 4 atoms / equivalent set). Note that italicised *T* in the t^γ column designates translations, while the non-italicised T designates the degeneracy of a particular symmetry species

	Aluminium (Al – D_{3d} (n=4))						
f^γ	t^γ	D_{3d} Site symmetry species containing translations	**correlations**	O^7_h - Factor group species	C_ζ	a_ζ	$\frac{a_\gamma}{a_{A_{2u}} + a_{E_u}}$
4	$1(T_z)$	A_{2u}		A_{2u}	1	1	1+0
8	$2(T_{x,y})$	E_u		E_u	2	1	0+1
				T_{1u} $(T_{x,y,z})$	3	2	1+1
				T_{2u}	3	1	0+1
$\Gamma_{Al} = A_{2u} + E_u + 2T_{1u} + T_{2u}$							

Table 4.3.1.7. Correlation between the T_d site group and the O^7_h factor group for the cobalt atoms (n = 2 atoms / equivalent set). Note that italicised *T* in the t^γ column designates translations, while the non-italicised T designates the degeneracy of a particular symmetry species

	Cobalt (Co – T_d (n = 2))						
f^γ	t^γ	T_d Site symmetry species containing translations	**correlations**	O^7_h - Factor group species	C_ζ	a_ζ	$\frac{a_\gamma}{a_{T_2}}$
6	$1(T_z)$	T_2		T_{2g}	3	1	1
				$T_{1u}(T_{x,y,z})$	3	1	1
$\Gamma_{Co} = T_{2g} + T_{1u}$							

Table 4.3.1.8. Correlation between the C_{3v} site group and the O_h^7 factor group for the oxygen atoms (n = 8 atoms / equivalent set). Note that italicised *T* in the t^γ column designates translations, while the non-italicised T designates the degeneracy of a particular symmetry species

	Oxygen (O – C_{3v} (n = 8))						
f^γ	t^γ	C_{3v} Site symmetry species containing translations	**correlations**	O_h^7 - Factor group species	C_ζ	a_ζ	$\frac{a_\gamma}{a_{A_{2u}} + a_{E_u}}$
8	1(T_z)	A_1		A_{1g}	1	1	1+0
16	2($T_{x,y}$)	E		T_{2g}	3	2	1+1
				A_{2u}	1	1	1+0
				$T_{1u}(T_{x,y,z})$	3	2	1+1
				E_g	2	1	0+1
				T_{1g}	3	1	0+1
				E_u	2	1	0+1
				T_{2u}	3	1	0+1
$\Gamma_O = A_{1g} + 2T_{2g} + A_{2u} + 2T_{1u} + E_g + T_{1g} + E_u + T_{2u}$							

When equation 4.6 is applied to the results in Tables 4.3.1.6, 4.3.1.7 and 4.3.1.8 and taking into account that acoustical modes need to be subtracted, the same character as the translations listed in the character tables results in the total irreducible representation of $CoAl_2O_4$:

$$\Gamma^{CoAl_2O_4}_{Vibration} = \Gamma^{CoAl_2O_4} - \Gamma^{acoustic} \qquad 4.7$$

$$\Gamma^{CoAl_2O_4}_{Vibration} = \Gamma_{Co} + \Gamma_{Al} + \Gamma_{O} - \Gamma^{acoustic} \qquad 4.8$$

Substituting with information from Tables 4.3.1.6, 4.3.1.7 and 4.3.1.8, and collecting terms, using the character tables,[13] to determine which modes will be active in Raman and/or infrared and which will be inactive in both, the required equation is readily obtained as:

$$\Gamma^{CoAl_2O_4}_{Vibration} = \{T_{2g} + T_{1u}\} + \{A_{2u} + E_u + 2T_{1u} + T_{2u}\} + \{A_{1g} + 2T_{2g} + A_{2u} + 2T_{1u} + E_g + T_{1g} + E_u + T_{2u}\} - T_{1u} \quad 4.9$$

or

$$\Gamma^{CoAl_2O_4}_{Vibration} = A_{1g}\,(R) + 3T_{2g}(R) + E_g(R) + 4T_{1u}\,(IR) + T_{1g} + 2A_{2u} + 2E_u + 2T_{2u} \quad 4.10$$

This predicts five Raman active modes ($A_{1g} + E_g + 3T_{2g}$). Both the synthesised pigment and that on the shards (Figure 4.3.1.1 (A and B)) show more Raman bands than the number predicted by group theory.

However, it is well known that cationic disorder in spinel compounds lowers the symmetry, thereby increasing the vibrational modes.[9] This may account in part for the additional bands observed for the cobalt blue spectrum from the shard. X-ray diffraction patterns (Figure 4.3.1.2) also show the spinel structured cobalt blue to be the only phase present in the pure synthsized cobalt blue samples (see also reference 7), and therefore it is expected that all the observed Raman bands from the pure synthesised samples will be those of cobalt blue. Figure 4.3.1.1 (B) is a typical spectrum of cobalt blue on the shard samples. The shoulder at about 410 cm^{-1} in Figure 4.3.1.1 (B) is due to cobalt blue.

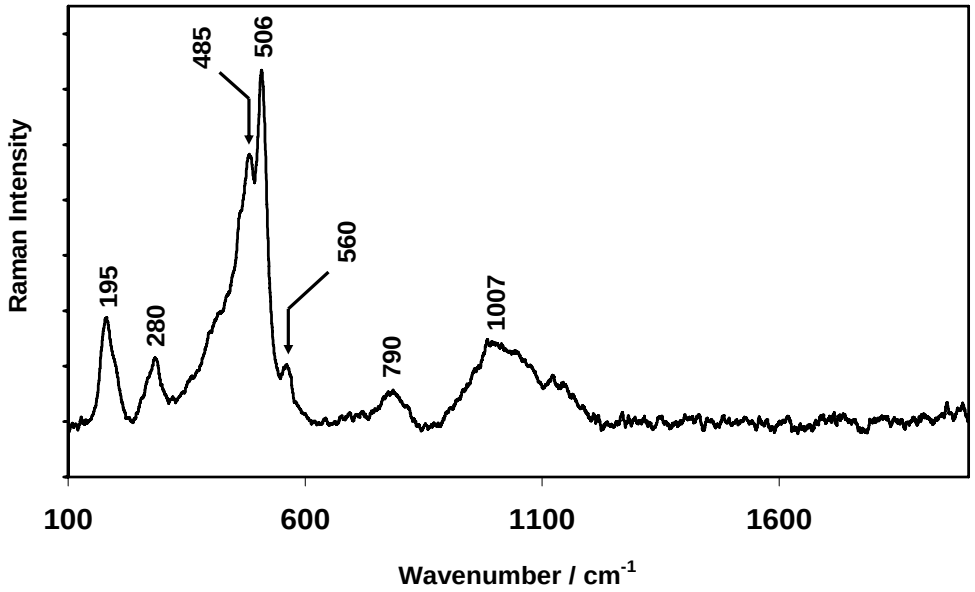

Figure 4.3.1.1. (B) A representative Raman spectrum of an underglaze blue pigment at the ceramic/glaze interface showing all the identified Raman bands. The broad band at 1007 cm^{-1} is due to the silicate glaze, while the shoulder at around 410 cm^{-1} (not labelled) is due to cobalt blue

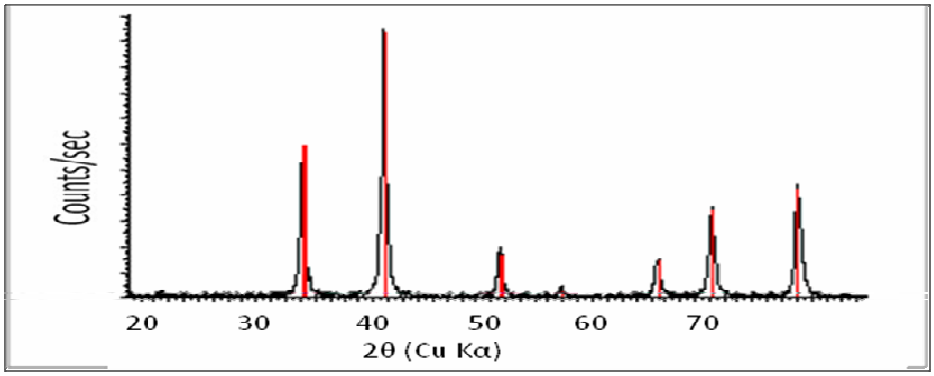

Figure 4.3.1.2. The figure shows an XRD pattern of synthesised cobalt blue showing cobalt blue as the only phase present in the sample. This sample was removed from the furnace and allowed to cool slowly

However, when a comparison is made between cobalt blue and a similar spinel ($MgAl_2O_4$) for which assignments have already been made,[11,15-17] a likely Raman band assignment for the cobalt blue is predicted to be as follows: 197 cm^{-1} ($T_{2g}(1)$), 508 cm^{-1} ($T_{2g}(2)$), 643 cm^{-1} ($T_{2g}(3)$), 409 cm^{-1} (E_g) and 769 cm^{-1} (A_{1g}) for the pure isolated pigment. The corresponding Raman bands of the blue pigment on the shards (Figure 4.3.1.1 (B)) are 195 cm^{-1} ($T_{2g}(1)$), 506 cm^{-1} ($T_{2g}(2)$), 690 cm^{-1} ($T_{2g}(3)$), 410 cm^{-1} (E_g) and 790 cm^{-1} (A_{1g}).

The additional Raman bands at 560 cm^{-1} and 485 cm^{-1} could be the result of differential cooling between the ceramic body and the glaze. Indications of tensile stress imposed on the interface by this phenomenon have been indicated by interfacial quartz in studies of glazed porcelain.[17] Figure 4.3.1.3 shows representative surface (glaze) and interfacial (ceramic/glaze) Raman spectra for the Meissen sample (the broken cup shown in Figure 4.1.3 (E)).

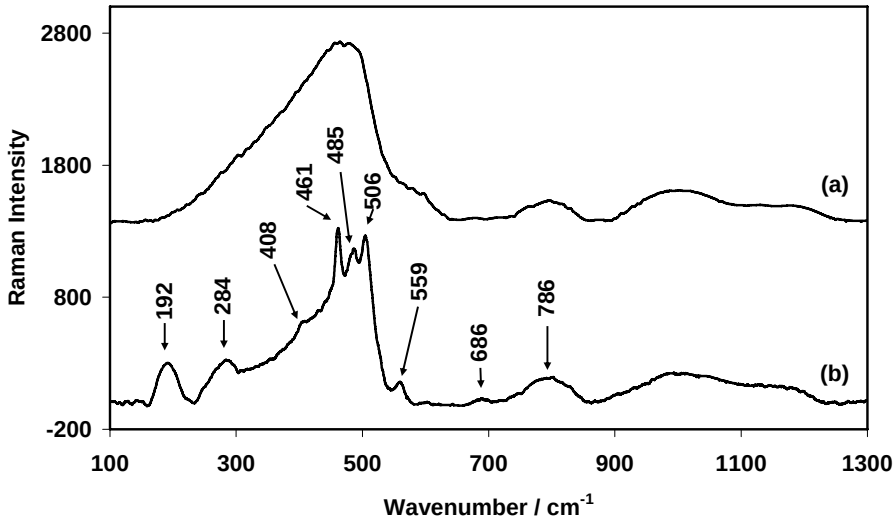

Figure 4.3.1.3. The surface (a) and interface (b) spectra for the Meissen sample E (Figure 4.1.3 (E)), is typical for all the blue and white porcelain blue pigment in our possession. The 461 cm^{-1} Raman band is attributed to α-quartz which is similar to all the blue and white porcelain in our study

4.3.2. Amorphous carbon

The Raman spectra of several samples show the presence of broad Raman bands around 1300 cm^{-1} and 1600 cm^{-1}, and these are attributed to amorphous carbon.[18] In considering a single crystal of graphite, factor group analysis[19] shows that this system belongs to the D^4_{6h} symmetry group and that the Brillouin zone centre modes can be decomposed into the following irreducible representation:[20]

$$\Gamma = A_{2u} + 2B_{2g} + E_{1u} + 2E_{2g} \qquad 4.11$$

The separation of these modes into Raman, infrared and inactive modes is shown in Table 4.3.2.1.

Table 4.3.2.1. The Raman, infrared and inactive modes of a single graphite crystal as compiled from the literature

Raman active	IR active	Silent in both[23]	Observed mode[21,22] (cm^{-1})
$E_{2g}(1)$	-	-	42
$E_{2g}(2)$	-	-	1581
	A_{2u}		867
	E_{1u}		1588
		$B_{2g}(1)$	127**
		$B_{2g}(2)$	Not observed

**Observed by neutron scattering.

The amorphous carbon that is found on the sample is present due to contact with the samples, either unintentionally through contamination or intentionally through its use as a black pigment on the artifact. Ancient black pigments that have been used on artifacts come from two broad categories, lamp black and ivory black. The latter

is being so called due to its origin from calcined bone or ivory.[24,25] Ivory black can usually be distinguished from lamp black in its Raman spectrum by a phosphate (PO_3^{2-}) feature at 960 cm^{-1} as a result of collagen from animal remains.[24] However, other work[19] has shown that some samples of ivory black often fail to show the phosphate Raman band. Therefore, the absence of the 960 cm^{-1} band cannot be used to exclude ivory black as the black pigment that is often found on ancient artifacts and also the samples under study in this work.

Typically, blue and white ceramic samples also show the presence of amorphous carbon on the surfaces of the glaze but not in the interior of the sample glaze (Figure 4.3.1.3).

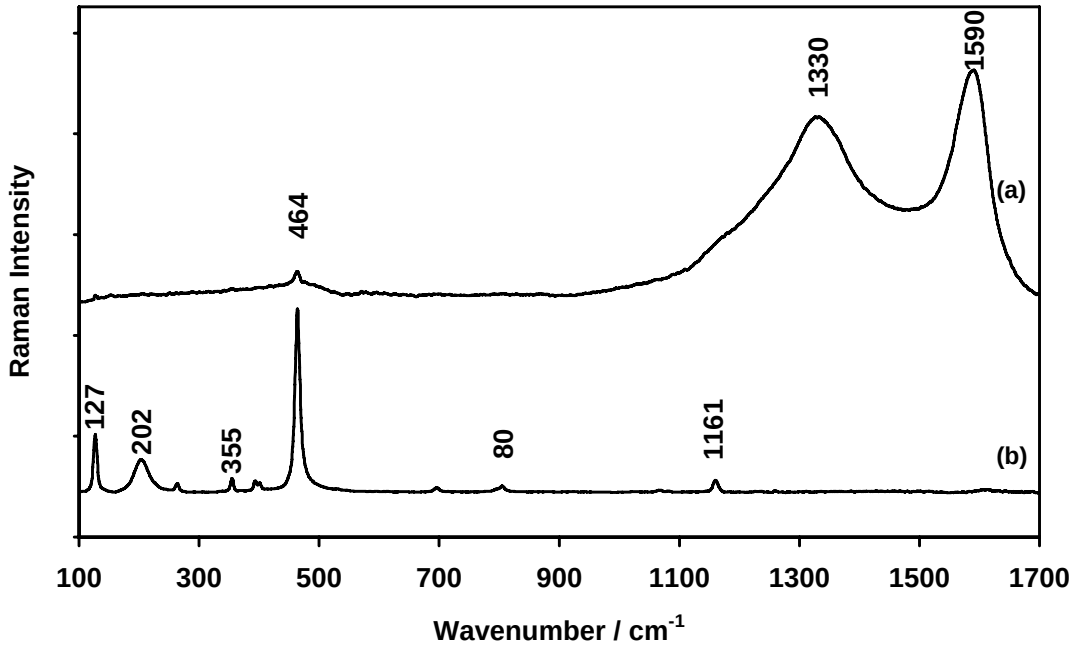

Figure 4.3.1.4. The surface of sample F (excavated cup) shows a thin layer of amorphous carbon (a) (0 µm), while less than 4 µm below the surface, the carbon disappears completely. This phenomenon is typical of all the samples in this study

The presence of amorphous carbon on the surfaces of these samples could be due to surface contamination during manufacturing. The amorphous carbon contamination is also predominant towards the bottom side of the artifact (dish, cup or plate), suggesting that the origin of the contaminated draft or gas may have been from the bottom of the saggar where the kiln fire is more likely to be located.

4.3.3. Anatase (TiO_2)

Anatase was detected on the surfaces of two of the shards of archaeological origin (Figure 4.1.3, (C and D)), as well as on the ceramic body of the Meissen shard sample (Figure 4.1.3, (E)). On samples C and D, anatase was detected at the interface below a thin layer of cobalt blue pigment presumed to have leached out of the blue glaze. A schematic view of the ceramic/glaze interface on the white background of samples C and D is shown in Figure 4.2.4.

Anatase is one of the three polymorphic forms of TiO_2; the other two are brookite and rutile.[26,27] However, all three have very distinct Raman band fingerprints. Only anatase and rutile were detected on these samples. However, brookite and its Raman band positions are discussed here for comparison with the other two TiO_2 polymorphs (anatase and rutile). While anatase shows a strong Raman band at 140 cm^{-1}, brookite shows a strong band at 153 cm^{-1} and rutile shows no such band.[28]

The anatase form is identified by Raman band assignments at 140 cm^{-1} (E_g), 197 cm^{-1} (E_g), 394 cm^{-1} (B_{1g}), 517 cm^{-1} (B_{1g}) and 637 cm^{-1} (E_g).[29,30] Figure 4.3.3.1(b) shows the full anatase Raman spectrum as identified on the body of the Meissen shard sample E. In other situations, once a full spectrum can be identified, it is usually sufficient to look for the intense 140 cm^{-1} (E_g) Raman band in and around the

same sample for positive identification of anatase. This is seen, for instance, for sample D in Figure 4.2.3(e) and (f) where anatase occurs with α-quartz[1].

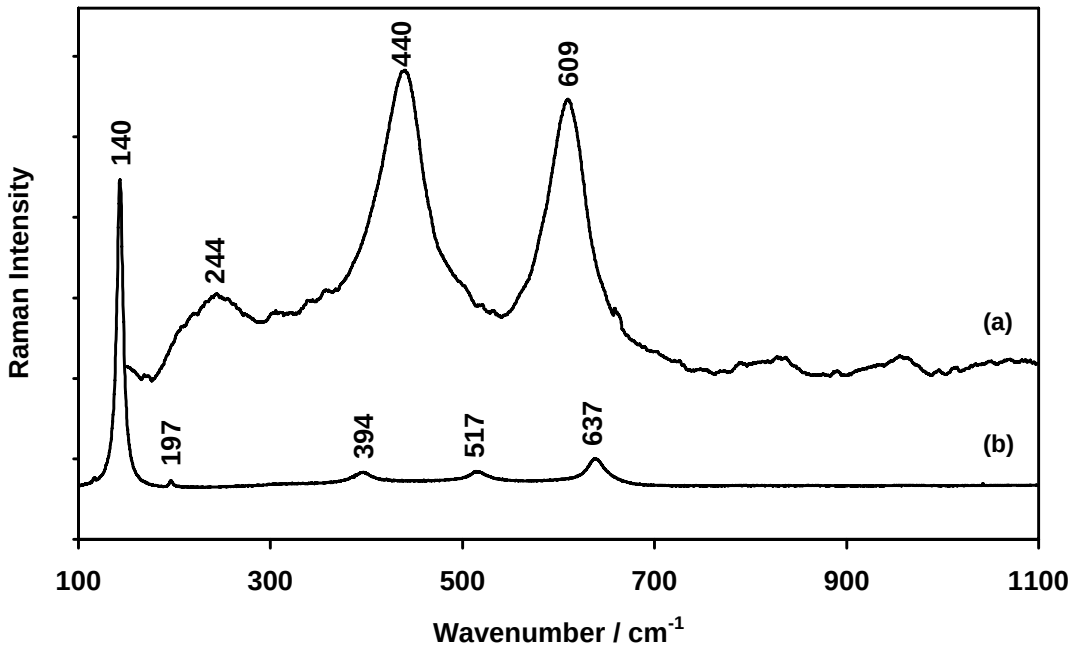

Figure 4.3.3.1. (a) Rutile (TiO_2) spectrum, with characteristic Raman bands at 244 cm^{-1} (A_{1g}), 440 cm^{-1} (E_g) and 609 cm^{-1} (B_{1g}), and (b) anatase (TiO_2) spectrum, with bands at 140 cm^{-1} (E_g), 197 cm^{-1} (E_g), 394 cm^{-1} (B_{1g}), 517 cm^{-1} (B_{1g}) and 637 cm^{-1} (E_g). Both (a) and (b) are recorded from the ceramic body of sample E (Meissen)

4.3.4 Rutile (TiO_2)

Rutile was also detected in the ceramic body of the Meissen sample E (Figure 4.3.3.1(a)). This TiO_2 polymorph was identified by its characteristic Raman bands at 244 cm^{-1} (A_{1g}), 440 cm^{-1} (E_g) and 609 cm^{-1} (B_{1g}). Anatase-to-rutile phase transformation[31,32] occurs between 800 ^oC and 1 100 ^oC. The presence of rutile in

the ceramic body of sample E suggests that temperatures of at least 800 ^{o}C were reached during the manufacture of the artefact.

However, what is interesting about the ceramic body of the Meissen sample (E) is that anatase (TiO_2), rutile (TiO_2) and mullite co-exist in the same ceramic body sample. The mullite ($2Al_2O_3 \cdot SiO_2$ or $3Al_2O_3 \cdot 2SiO_2$) detected in the ceramic body indicates the use of kaolinite minerals as starting materials since temperatures above 1 200 ^{o}C are required for these kaolinite/mullite transformations.

Also, Meissen ceramic body samples have already been confirmed to have been sintered at these high temperatures.[33] However, at these temperatures, it is expected that anatase (TiO_2) should be converted to rutile (TiO_2), its high-temperature polymorphic form.

The answer to this may lie in the mechanism of anatase/rutile phase transformation itself. It has already been shown that the reduced nucleation probability of anatase could impede the anatase-to-rutile phase transformation past the critical temperature.[34] It should be noted that this phase transformation can also be influenced by the presence of other materials in the sample.[1] This point needs further investigation as this work continues.

4.3.5 Hematite (α-Fe_2O_3)

Hematite was detected only as part of the brown line at the bottom of one of the Ming shard samples, B (Figure 4.3.4.1). This pigment was identified through some of its characteristic Raman bands and their assignments[35] at 221 cm^{-1}(A_{1g}), 294 cm^{-1} (E_g), 409 cm^{-1} (E_g) and 601 cm^{-1} (E_g) (Figure 4.3.4.2).

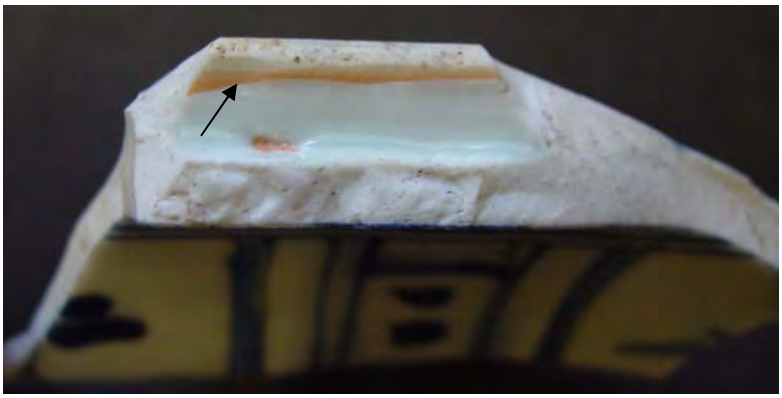

Figure 4.3.5.1. The brown line at the bottom of Ming sample B is indicated with an arrow. This line is more prominent on the inside bottom than the outside bottom where it appears to have been scraped off

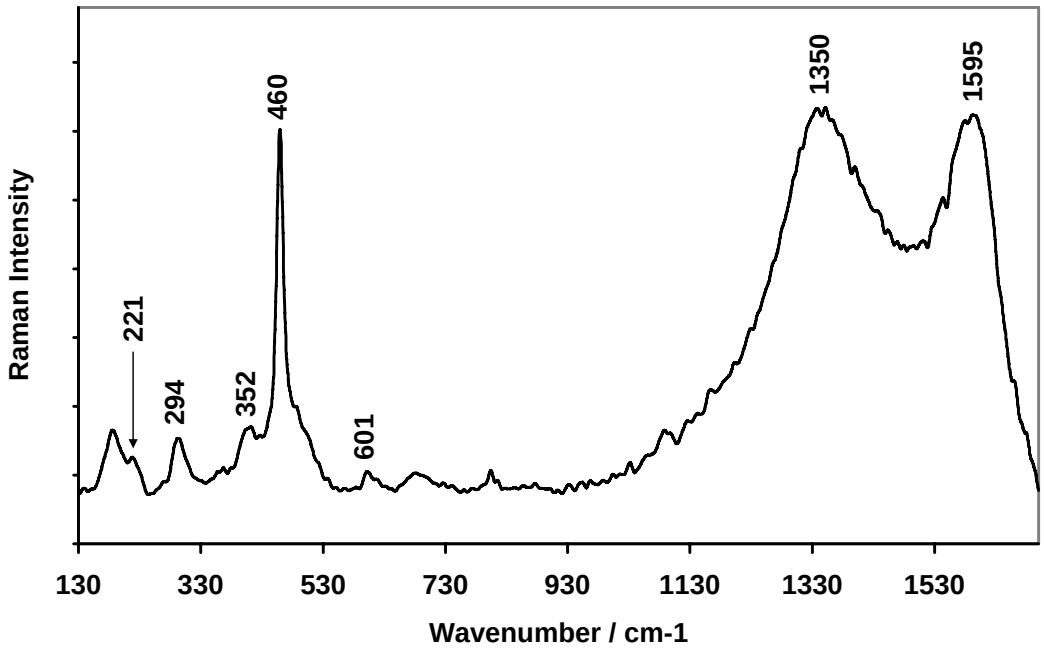

Figure 4.3.5.2. Spectrum showing typical α-Fe_2O_3 Raman bands at 221 cm^{-1} (A_{1g}), 294 cm^{-1} (E_g), 409 cm^{-1} (E_g) and 601 cm^{-1} (E_g) as collected directly from the brown line of sample B, indicated with an arrow in Figure 4.3.4.1

In this case it was found mixed with amorphous carbon appearing as broad Raman bands at 1350 cm^{-1} and 1595 cm^{-1}. The intense band at around 460 cm^{-1} is attributed to α-SiO_2.

This brown line is similar to what has been called “the chocolate bottom” on Vietnamese porcelain.[36] Many explanations have been put forward as to its existence. It is believed that these could be deliberate markings or an adhesion substance to prevent the item from sticking to the saggar.[36] In this case, the brown line could be contamination, as it appears that it was scraped off the outside of the artifact.[1]

4.3.6 Mullite ($2Al_2O_3{\cdot}SiO_2$ or $3Al_2O_3{\cdot}2SiO_2$)

Mullite is part of a broader group of materials that have recently gained attention due to the possibility of their application in solid oxide fuel cells,[37] oxygen sensors and gas separation membranes,[38,39] in addition to their traditional ceramics applications. The detection of mullite in the ceramic body of the Meissen sample is consistent with studies in other laboratories.[40] A representative mullite spectrum as collected from the Meissen sample (sample shown in Figure 4.1.3 (E)) is shown in Figure 4.3.5.1. The large number of Raman bands on this spectrum does not come as a surprise. Vibrational analysis of mullite, using group theory, shows that as many as 42 Raman-active vibrational modes are possible,[41] as shown in equation 4.12:

$$\Gamma_{\text{Raman}} = 12A_g + 12B_{1g} + 9B_{2g} + 9B_{3g} \qquad 4.12$$

Mullite was also detected in the ceramic body of Ming samples A and B, but only after a piece of the ceramic body had been ground into powder and moulded into a

smooth surface; a 100X objective lens was used to collect the spectra as has been successfully done elsewhere.42

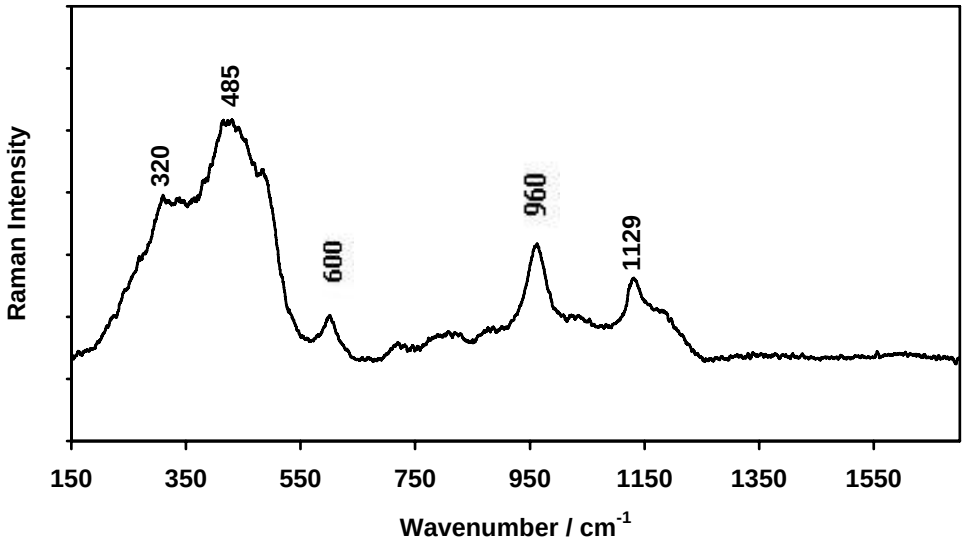

Figure 4.3.6.1. Spectrum of mullite in the ceramic body of the Meissen sample (Figure 4.1.3 (E)) with Raman bands at 320 cm^{-1}, 485 cm^{-1}, 600 cm^{-1}, 960 cm^{-1} and 1129 cm^{-1}

4.4 Intact plates

This section deals with the studies on the intact plates. These include two known museum intact plates of Ming dynasty origin and an unknown museum intact plate that appears to have gone through quite substantial restoration recently. The artifacts will be discussed in that order.

4.4.1 Ming dynasty plates Hongzhi (1488–1505) and Wanli (1573–1620)

The glaze depth profiling method that was used to study the Ming and Meissen artifacts and those of unknown origin was also applied to intact Ming dynasty plates

from the J.A. van Tilburg Museum of the University of Pretoria. The plates are of the Ming dynasty but from two distinct periods (Hongzhi (1488–1505) and Wanli (1573–1620)) within the Ming dynasty and are shown in Figure 4.1.3, (H) and (I) respectively.

Figures 4.4.1.1 and 4.4.1.2 show the Raman spectra collected from the ceramic/glaze interface of the two plates compared with those collected from the glaze surfaces. The blue pigment was then identified as $CoAl_2O_4$ in these Ming plates without the pigment being exposed to the surface.

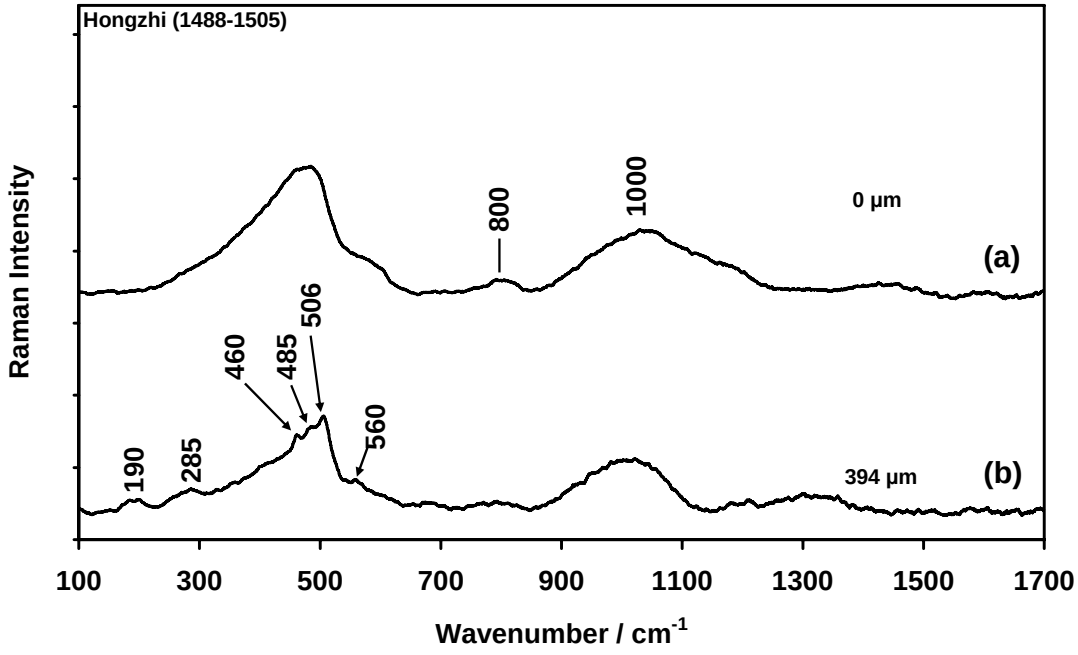

Figure 4.4.1.1. Surface (a) and interface (b) spectra for the Ming plate (Hongzhi (1488 – 1505)) shown also in Figure 4.1.3 (H). Note the glaze thickness of about 390 µm

Cobalt blue or cobalt aluminium oxide ($CoAl_2O_4$) is the origin of the blue colour in the Ming plates. The blue pigment on these plates was not mixed with amorphous

carbon as was the case with the other Ming shards. This is in contrast to the blue pigment on the archaeological shards which was mixed with amorphous carbon.

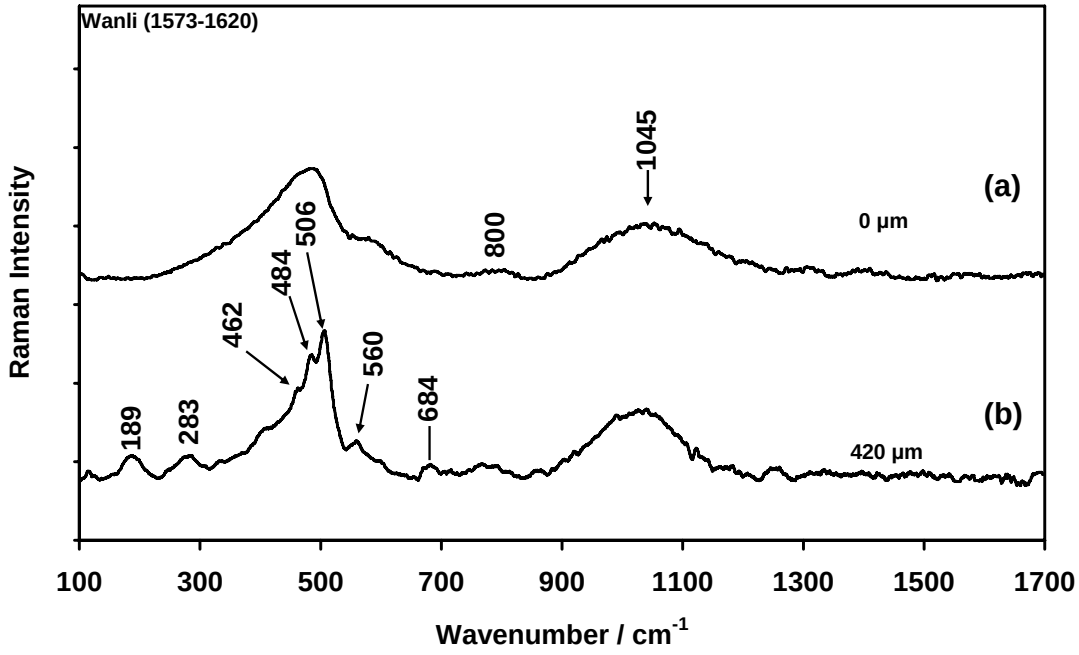

Figure 4.4.1.2. Surface (a) and interface (b) spectra for the Ming plate (Wanli (1573–1620)) shown also in Figure 4.1.3 (I). Note the glaze thickness of about 420 µm on this plate

Many more micro-Raman studies of Ming plates need to be undertaken in order to establish whether the lack of amorphous carbon in the blue pigment of these Ming samples was commonplace during the Ming period, or whether the samples under study in this work are exceptions.

4.4.2 Unknown intact plate

Unlike the Ming plates, this plate (Figure 4.4.2.1), although similar to the Ming dynasty plates, seemed to have been extensively restored and repainted.

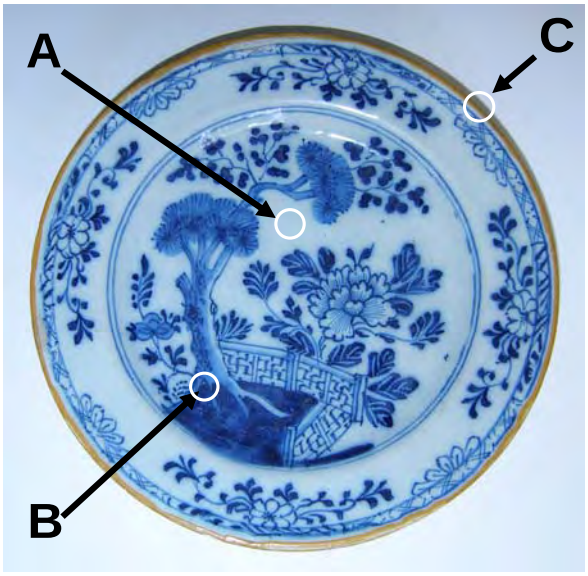

Figure 4.4.2.1. Unknown intact plate, showing the various positions chosen for study

Figure 4.4.2.2 shows the glaze depth profile Raman spectra on the white background of the unknown plate (position A in Figure 4.4.2.1). The white background clearly reveals a white SnO_2; the broad Raman bands around 500 cm^{-1} and 1000 cm^{-1} are attributed to the silicate glaze.

The presence of amorphous carbon on the surface of the glaze, as indicated by the doublet at around 1300 cm^{-1} and 1600 cm^{-1}, was noted. The presence of amorphous carbon is typical of all the ceramic artifacts that were chosen for study,

both the known or unknown museum specimen artifacts and those of archaeological origin.

A dark blue background (position B in Figure 4.4.2.1) was chosen for the glaze depth profile studies.

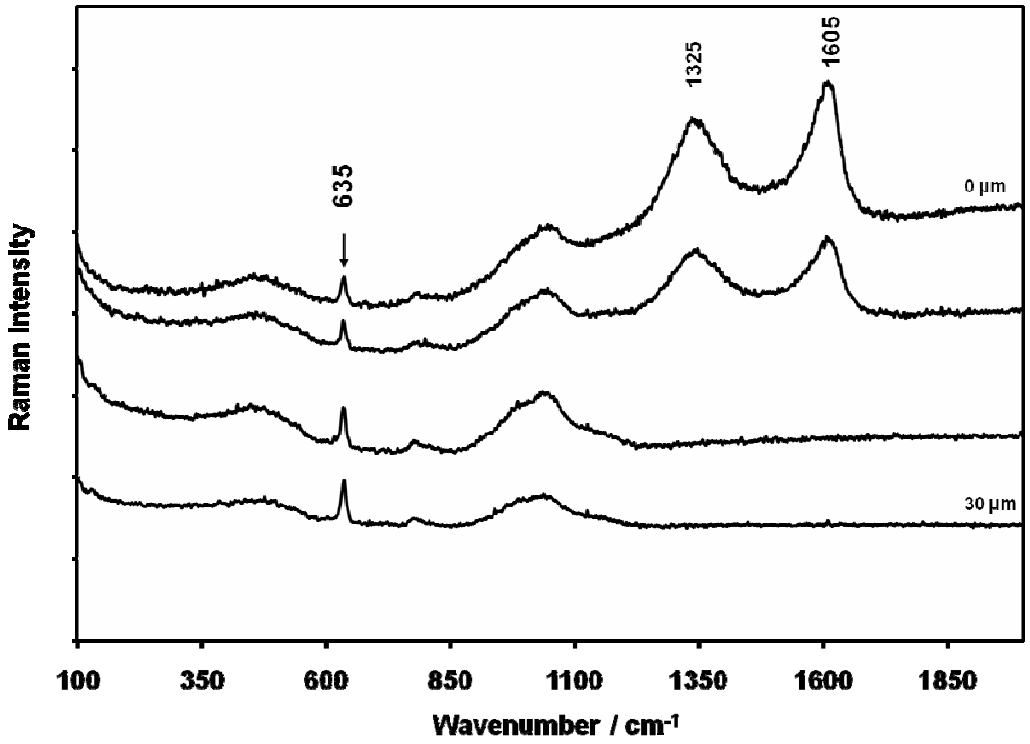

Figure 4.4.2.2. Glaze depth profile showing a predominantly cassiterite (SnO_2) glaze (position A in Figure 4.4.2.1). The blue pigment is not detected here despite the visibly blue glaze

The results (Figure 4.4.2.3) reveal a pigment that is spread from the surface to the interior of the glaze rather than at the ceramic/glaze interface. This pigment is

similar to the olivine/willemite type (Co_xZn_{2-x} SiO_4 with $0 \leq x \leq 2$) pigments with a strong Raman band at 823 cm^{-1}, as reported in the literature.[41,43] The spectrum also shows three less intense Raman bands in the region 300 cm^{-1} to 500 cm^{-1} (Figure 4.4.2.3).

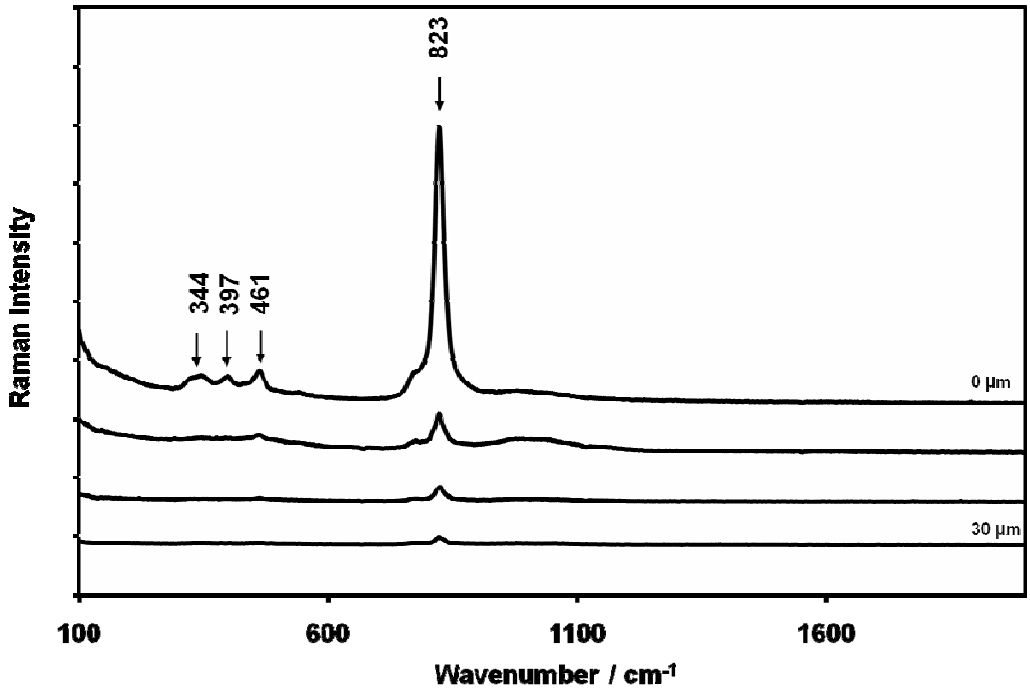

Figure 4.4.2.3. Glaze depth profile for the unknown plate (position B in Figure 4.4.2.1). The blue pigment on this plate shows that it has an olivine-type pigment and is more intense on the glaze surface rather than the glaze interior

Position C in Figure 4.4.2.1 consists of a "golden" or brown-yellow pigment laid on the surface of the artifact's rim. Raman spectroscopy consistently shows this "golden" rim to be composed of the rutile phase of TiO_2, trace amounts of calcite ($CaCO_3$) and the anatase phase of TiO_2. These pigments point to a more modern restoration effort on this unknown museum piece. Firstly, should one argue that the rutile on the rim is due to an originally applied naturally occurring anatase, which

was then sintered at temperatures of between 800 ^{o}C and 1100 ^{o}C, other impurities associated with natural anatase should still be present. No other impurity (other than traces of $CaCO_3$) was detected in the rim.

Secondly, it was only early in the last century that industrial processes were developed[29] for the manufacture of pure anatase (1923) and rutile (1947).

More studies will have to be conducted to obtain more detailed chemical information on this artifact, including the correct identification of the type of olivine pigment. Nevertheless, the depth profiling method applied in this work opens a new avenue for research in the area of art and archaeology.

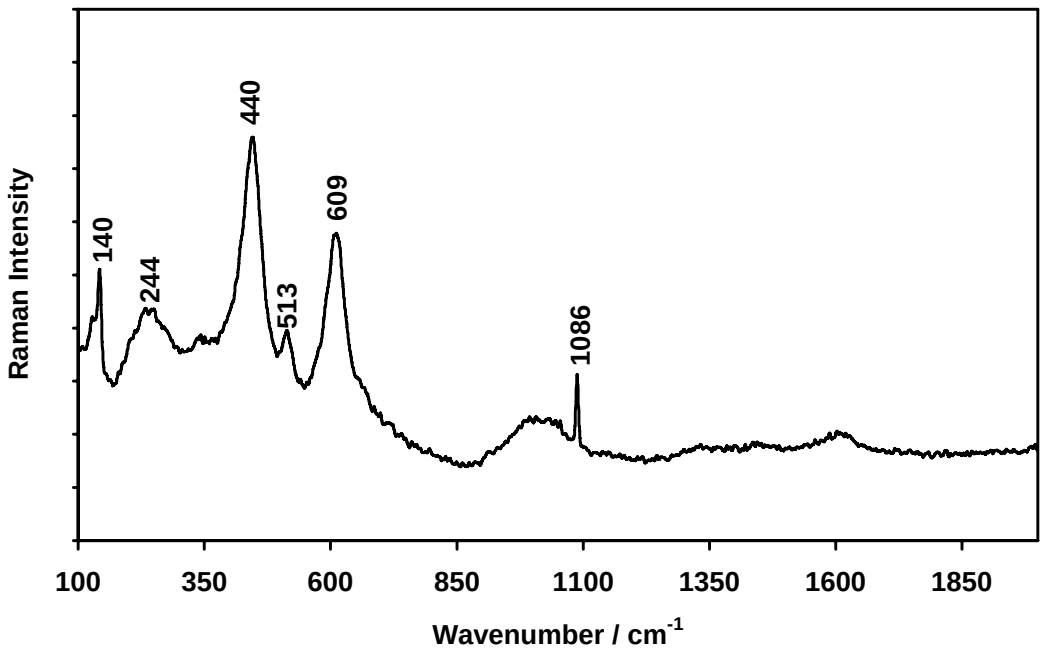

Figure 4.4.2.4. Raman spectrum of the “golden” rim, showing rutile as the main component as indicated by the main Raman bands with traces of anatase (140 cm^{-1}) and $CaCO_3$.(1086 cm^{-1})

4.5 Conclusion

The porcelain glaze depth profile studies on intact plates that have been presented in this chapter provide a unique method for probing ceramic/glaze interfacial pigments by focusing the laser beam through the glaze. Laser powers of about 20 mW to 40 mW were used to probe porcelain glazes of 0.1 mm to about 0.4 mm. Interfacial layer structure was constructed from the Raman spectra obtained directly from the interface. Pigment identification and characterisation were therefore possible and in some cases the type and composition of these pigments may lead to conclusive cut-off dates for manufacturing.

In the case of the discovery of pure white anatase, the manufacturing date was placed after the 1920s, which is the date of first manufacture of pure white anatase. Cobalt blue ($CoAl_2O_4$), anatase (TiO_2), rutile (TiO_2), hematite (α-Fe_2O_3), mullite ($2Al_2O_3{\cdot}SiO_2$ or $3Al_2O_3{\cdot}2SiO_2$), amorphous carbon and an olivine/willemite type of compound were identified on the blue ceramic shards and plates that were studied. This study has established a benchmark on the study of ceramic/glaze interfacial pigments by focusing visible laser radiation through the glaze using confocal micro-Raman spectroscopy.

However, the success of this method on silicate-based glazes, such as the blue and white shards that have already been studied, does not necessarily extend to the SnO_2-based glazes that were also commonly used in ancient times. A study on a tile shard from the Citadel of Algiers with a predominantly SnO_2-based glaze will be presented in Chapter 5. This is expected to validate or invalidate the use of the glaze depth profile method on samples of this type, while gathering information that could be used in reconstruction and preservation work on ancient objects of cultural significance.

4.6 References

1. Kock, L.D. and de Waal, D. *J. Raman Spectrosc*. 2007, **38**, 1480.
2. Clark, R.J.H., Wang, Q. and Correia, A. *J. Archaeol. Sci*. 2007, **6**, 1.
3. Colomban, P., Milande, V. and Lucas, H. *J. Raman Spectrosc*. 2004, **35**, 68.
4. Baraldi, P. and Tinti, A. *J. Raman Spectrosc*. 2008, **39**, 963.
5. Luchesi, S. and Delta Guista, A. *Minel. Petrol*. 1997, **59**, 91.
6. Schiessl, W., Poltzel, W., Karzel, H., Steiner, M. and Kalvius, G.M. *Phys. Rev*. *B*. 1991, **53**, 9143.
7. Yu, N., Sickafus, K.E. and Nastasi, M. *Phil. Mag. Lett.* 1994, **70**, 235.
8. Zinkle, S.J. *J. Nucl. Mater*. 1995, **219**, 113.
9. Melo, D.M.A., Cunha, J.D., Fernandes, J.D.G., Bernardi, M.I., Melo, M.A.F. and Martinelli, A.E. *Mater. Res. Bull.* 2003, **38**, 1559.
10. De Waal, D. *J. Raman Spectrosc*. 2004, **35**, 646.
11. Li, W., Li, J. and Gua, J. *J. Eur. Ceram. Soc*. 2003, **23**, 2289.
12. Thibaudeau, P. *J. Phys.: Condens. Matter*. 2002, **14**, 3543.
13. Fateley, W.G., Dollish, F.R., McDevitt, N.T. and Bentley, F.F. *Infrared and Raman Selection Rules for Molecular and Lattice Vibrations: The Correlations Method,* New York, Wiley-Interscience, 1971.
14. Borel, A. *Linear Algebraic Groups, Graduate Text in Mathematics,* 2nd edition. Berlin, New York, Springer-Verlag, 1971.
15. Wang, Z., Schiferl, D., Zhao, Y. and O'Niell, H.St.C. *J. Phys. Chem*. *Solids*. 2003, **64**, 2517.
16. Malezieux, J.M. and Birious, B. *Bull Mineral*. 1988, **111**, 649.

17. Thibaudeau, P. and Gervais, F. *J. Phys.: Condens. Matter*. 2002, **14**, 3543.

18. Kawashima, Y. and Katagiri, G. *Phys. Rev*. B. 1995, **14,** 53.

19. Mani, K.K. and Ramani, R. *Phys. Status. Solidi*. 1974, **B61**, 659.

20. Kawashima, Y. and Katagiri, G. *Phys. Rev. B* 1995, **14,** 52.

21. Nemanich, R.J. and Solin, S.A. *Phys. Rev. B.* 1979, **20**, 392.

22. Nemanich, R.J., Lucovsky, G. and Slin, S.A. *Mater. Sci. Eng*. 1977, **31**, 157.

23. Nieklow, R., Wakabayashi, N. and Smith, H.G. *Phys. Rev. B*. 1972, **5**, 4951.

24. Smith, G.D. and Clark, R.J.H. *J. Archaeol. Sci*. 2004, **31**, 1137.

25. Edwards, H.G.M. *J. Raman. Spectrosc*. 2000, **31**, 407.

26. Clark, R.J.H., Cridland, L., Kariuki, M.B., Harris, K.D.M. and Withnall, R. *J. Chem. Soc. Dalton Trans*. 1995, 2577.

27. Clark, R.J.H. *The Chemistry of Titanium and Vanadium.* Amsterdam, Elsevier, 1968.

28. Cassaignon, S., Koelsch, M. and Jolivet, J-P. *J. Mater. Sci*. 2007, **42**, 6689.

29. Burgio, L. and Clark, R.J.H. *J. Raman Spectrosc*. 2000, **31**, 395.

30. Miao, L., Tanemura, S., Toh, S., Kaneko, K. and Tanemura, M.J. *J. Crystal Growth.* 2004, **264**, 246.

31. Colomban, P. and Mazerolles, L. *J. Mater. Sci.* 1991, **26**, 3503.

32. Kim, D-W., Kim, T-G, and Hong, K.S. *J. Am. Ceram. Soc*. 1998, **81**, 1692.

33. Colomban, P*. J. Non-crystalline Solids*. 2003, **323**, 180.

34. Zhang, H. and Banfield, J. F. *J. Mater. Res*. 2000, **15**, 437.

35. De Faria, D.L.A., Venancio, S. and de Oliviera, M.T. *J. Raman Spectrosc.* 1997, **28**, 873.

36. Colomban, P., Liem, N.Q., Sagon, G., Tinh, H.X. and Hoah, T.B. *J. Cult. Herit*. 2003, **4,** 187.

37. Beran, A., Libowitzky, E., Burianek, M., Muhlberg, M., Percharroman, C. and Schneider, H. *Cryst. Res. Technol*. 2008, **43**, 1230.

38. Zha, S., Cheng, J., Liu, Y., Liu, X. and Meng, G. *Solid State Ionics.* 2003, **156**, 197.

39. Goodenough, J.B. *Ann. Rev. Mater*. 2003, **33,** 91.

40. Colomban, P. and Milande, V. *J. Raman Spectrosc*. 2006, **37**, 606.

41. Cui, H., Zayat, M. and Levy, D. *Chem. Mater*. 2005, **17**, 5562.

42. Liem, N.G., Sagon, G., Quang, V.X., Tan, H.V., Colomban, P. *J. Raman Spectrosc.* 2000, **31**, 933.

43. Fores, A., Llusar, M., Badenes, J.A., Calbo, J., Tena, M.A. and Monros, G. *Green Chem*. 2000, **2**, 93.